Performance assessment of SVM-based classification techniques for the detection of artificial debondings within pavement structures from stepped-frequency A-scan radar data

Shreedhar Savant Todkar, Cédric Le Bastard, Vincent Baltazart, Amine Ihamouten, Xavier Dérobert

Version of Record: https://www.sciencedirect.com/science/article/pii/S0963869518306960
Manuscript_a168290e95212d1adefb4927d7bdfde8

Performance assessment of SVM-based classification techniques for the detection of artificial debondings within pavement structures from Stepped-frequency A-scan radar data

Shreedhar Savant Todkar[a,b,*], Cédric Le Bastard[a], Vincent Baltazart[b], Amine Ihamouten[a], Xavier Dérobert[b]

[a] *Project team ENDSUM: Centre for Studies and Expertise on Risks, Environment, Durability, and Urban and Country Planning (Cerema), 23 Avenue Amiral Chauvin, 49130 Les Ponts-de-Cé, France*
[b] *The French Institute of Science and Technology for Transport, Development and Networks (IFSTTAR), route de la Bouaye, 44340 Bouguenais, France*

Abstract

Owing to traffic and weather conditions, pavement structures may suffer from horizontal and vertical cracks that shorten the overall lifetime of roadways. In this paper, we focus on the detection of the horizontal subsurface cracks (debondings) occurring between the first two pavement layers from Stepped-frequency Radar (SFR) data. The processing of radar data requires some refined signal analysis to detect constructive interference between overlapping echoes. It is performed from timely data by a supervised machine learning method namely, Support Vector Machines (SVM) and compared to the conventional reference method, namely, the amplitude ratio test (ART), which is routinely performed at the operational level. Besides, the straightforward application of SVM on raw data is compared to the solution using physical signal features (global and local) that reduces the computational burden. Performance assessment and comparison of the processing methods are conducted on data collected on a specific test-site with three different types of artificial debondings.

Keywords: Pavements, thin debondings, amplitude ratio test, supervised machine learning, Support Vector Machines, Stepped-frequency radar, detection.

1. Introduction

Roadways are one of the most widely spread network of transportation across the world. As of 2014, in France alone, roadways stretched over a million kilometers. Most of these roads are made up of multi-layered bituminous concrete and were laid over three decades ago. Over time, traffic and environmental factors may lead to sub-surface cracks at the interface between the top two stratified layers. These horizontal cracks are called *debondings*. Fig. 1 presents a simplified scheme of such a debonding occurring between the first two layers. Since these precarious defects occur sub-superficially, they tend to go unnoticed to visual control for a while. However, they may also give rise to interlayer stripping and/or reflexive cracks (leading to open cracks at the surface).

This mechanical behavior of the pavement mainly relies on parameters such as the transmission of stress and displacement across different pavement layers [1]. As such, in case of debonding between the asphalt layers, this greatly reduces the service life of the structure [2]. Thus, it is of great importance to conduct early detection of these defects to avoid worsening of structural pavement conditions with time.

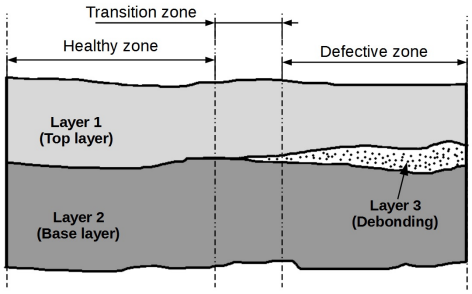

Figure 1: A representation of debonding occurring in a pavement structure

Over the past decades, several methods have been proposed to detect and survey the pavement structures. They can be broadly categorized into Destructive Testing (DT)

*Corresponding author
Email addresses: shreedhar.todkar@cerema.fr (Shreedhar Savant Todkar), cedric.lebastard@cerema.fr (Cédric Le Bastard), vincent.baltazart@ifsttar.fr (Vincent Baltazart), amine.ihamouten@cerema.fr (Amine Ihamouten), xavier.derobert@ifsttar.fr (Xavier Dérobert)

and Non-destructive Testing (NDT) [3]. In DT, a small section of the pavement structure is extracted by coring and analyzed for thicknesses estimation and anomalies characterization. Although DT readily provides visual information about the structure, it has obvious limitations due to its destructive nature. DTs are limited by number of times they can be performed and are not appropriate for routine pavement surveys [4]. Moreover, DTs provide a partial assessment of the pavement structure owing to the sparse spatial sampling of the coring process.

To overcome these drawbacks, NDT techniques have been introduced to survey structures and materials without damaging the Material Under Test (MUT) in any way. They have benefited from broad progress in remote sensing techniques. Due to its non-damaging ability, NDT is used in numerous applications including (but not restricted to) monitoring in monument degradation [5, 6], structural integrity tests [7], mechanical equipment testing [8], structural health monitoring and pavement monitoring [3].

The NDT methods rely on the capability of waves (mechanical, electromagnetic, vibrations) to probe the MUT for integrity, composition, homogeneity and other properties. Ground Penetrating Radar (GPR) is a well-known electromagnetic NDT method to probe dielectric materials. GPR uses radar pulses to obtain sub-surface information of a structure by mapping it into an image along the scanning direction. It uses the frequencies in the microwave band (wavelength are in order of a few centimeters in free space) to measure the reflected signals from the sub-surface structures. GPR is advantageous for subsurface monitoring as it is highly sensitive to the changes in the material permittivity, porosity and the water content. [9] reviews a three-decade journey of the GPR application in Civil engineering from testing and evaluation to diagnosing the pavement structures.

In the field of pavement monitoring, GPR has been used to estimate the thickness of pavements, detect debondings [10, 11, 12] and identify buried objects such as antipersonnel mines [13, 14], steel bars in concrete [15, 16] *etc.* However, as mentioned in [3], each of these applications require suitable processing methods to help at data interpretation and decision making (classification, identification *etc.*).

Since the past few decades, data-driven processing techniques have been challenging the conventional and model-based processing techniques. Among the former, machine learning methods (MLMs) have strongly emerged and are now widely used in the NDT domain along with GPR and other NDT methods [17, 18]. The GPR MLMs can be classified as supervised, semi-supervised and unsupervised methods. Under supervised methods, a part of the data is used to "learn" and then the remainder of the data is processed accordingly using the parameters obtained during "training" phase. Examples for supervised methods are Support Vector Machines (SVM), Artificial Neural Networks (ANN) [19], Naïve Bayes' theorem [20] *etc.* Unsupervised methods do not involve a training stage and the processing is done on the basis of clustering. These methods infer the results based on a set classification labels for the input data. Some examples of unsupervised methods are: k-means clustering, hierarchical clustering, mixture models *etc*. On the contrary, as mentioned in [21], the semi-supervised method is a mixture of the traditional supervised and unsupervised methods.

In this paper, we propose to use two processing methods namely, Amplitude Ratio test (ART) and Support Vector Machines (SVM) to detect thin debondings. ART is a characteristic-based reference method used to detect delaminations between pavement interfaces at the operational level. As mentioned in [22, 23, 24], the spatial variation in the magnitude of the second reflected echo along the scanning direction is used to detect delamination. ART is an easy-to-implement method which relies on only two signal features (*i.e.* magnitude or amplitude range). By contrast, SVM is a supervised machine learning method that may use several signal features for classification purposes. SVM first "learns" the classification using a set of labelled data and defines a classification model. During the testing stage, SVM uses the model and its parameters to detect debondings in the test data.

SVM sensitivity analysis is performed to observe the robustness of the method and also to analyze its dependency on the parameters such as kernel type, signal features, training data size *etc.*

This article is organized as follows: Section. 2 presents the experimental data that are used in this paper. In Section. 3, refined signal analysis is performed to characterize the debonding and non-debonding signals. We then present the two methods, ART and SVM in Section. 4. This section also discusses preprocessing steps for the proposed methods. Section. 5 compares the detection results on experimental data. In Section. 5.3, sensitivity analysis is carried out for SVM. In the final section, conclusions are drawn.

2. Experimental data

In this section, we present the experimental data acquired to test the proposed data processing methods. The data are collected using an SFR at IFSTTAR's fatigue carousel, a test-site dedicated to accelerate pavement testing over time and traffic.

2.1. The Fatigue Carousel

IFSTTAR's fatigue carousel is a $120\,\mathrm{m}$ long and $6\,\mathrm{m}$ wide one-off circular outdoor test track set up at the Nantes facility (Fig. 2). The carousel facilitates various

loading stages (65 kN on single wheel, twin wheel, tandem or tridem axles) with various configurations and speeds (up to 100 km/h) to reproduce the effect of in-use traffic at accelerated rate.

Figure 2: Fatigue carousel at IFSTTAR [11]

A quarter section of this track, approximately 25 m long, is dedicated to our experiments. This section of the pavement consists of a two-layered structure with the top layer (course layer) of about 5 cm to 6 cm thickness and the base layer of about 8 cm thickness over a granular sub-base. Three types of artificial defects are introduced between the course and the base layers. The rectangular patches marked $[A, a]$, $[B, b]$ and $[C, c]$ shown in Fig. 3, represent the defective regions over which the radar data were collected at the different loading stages. $[a]$, $[b]$ and $[c]$ are 2 m wide and 0.5 m long patches, and centered on the radius of 16 m; $[A]$, $[B]$ and $[C]$ are bigger debonded areas, 2 m wide by 1.5 m long. Other small patches, 50 cm $\times$ 50 cm, are located in and outside the wheel paths.

The three defects are Sand ($[A, a]$), Geotextile ($[B, b]$) and Tack-free based ($[C, c]$) respectively. The Geotextile based defects are supposed to represent somehow an ideal case study with the strongest radar signatures. By contrast, the Tack-free defects closely resemble a realistic defective pavement structure for which the two successive layers are not consolidated with some coating anymore. The relative permittivities ($\varepsilon_{r,mat}$) of artificial defects are related as $\varepsilon_{r,geo} > \varepsilon_{r,sand} > \varepsilon_{r,tf}$. Permittivities may be reinforced by water seeping with time, especially for geotextile because of some water trapped inside. Each debonding layer is of thicknesses (th_{mat}) between 0.5 cm to 1 cm, *i.e.*, smaller than $\lambda_{mat}/4$ (where λ_{mat} is the wavelength in the debonding layer). They are roughly related as $th_{geo} \approx th_{sand} > th_{tf}$. Finally, the rest of the carousel section corresponds to an healthy pavement structure, which is characterized by a perfect coating between layers and a small dielectric contrast between them.

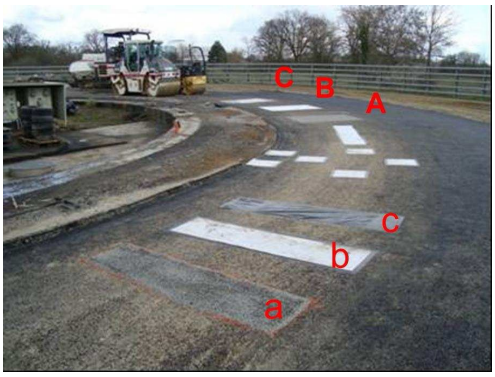

Figure 3: 25 m track with artificial defects [11] before laying the wearing course layer. Areas 'A,a', 'B,b' and 'C,c' indicate Sand, Geotextile and Tack-free based defects respectively

The measurements for each type of defect are taken at 10 thousand, 50 thousand, 100 thousand, 200 thousand, 250 thousand and 300 thousand cycles of the carousel (we will, from hereon represent the thousands of cycles as kcycles). These measurements (at different intervals) are expected to show some evolution in the signals over the defective regions due to increased use of traffic over time.

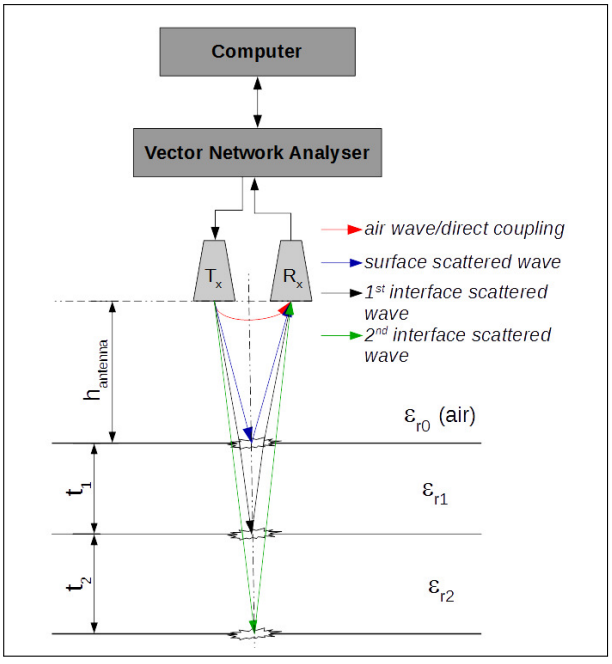

Figure 4: SFR configuration

2.2. *Stepped-frequency Radar data collection*

The Stepped-Frequency Radar (SFR) used for the data collection over the fatigue carousel is an experimental Ultra Wide-Band (UWB) radar. Data are collected in frequency domain within the bandwidth 0.8 GHz to

10.8 GHz using a Vector Network Analyzer (VNA) [25]. Inverse Fourier Transform is conventionally used to provide radar data in time domain.
The transmitter (Tx) and Receiver (Rx) are air-coupled exponentially tapered slot antennas (ETSA) [26] positioned in bi-static configuration with $dist_{tr} = 20\,\mathrm{cm}$, and offset at a height $h_{antenna} = 40\,\mathrm{cm}$ above the pavement surface. Fig. 4 shows the configuration scheme for SFR during the experiments.

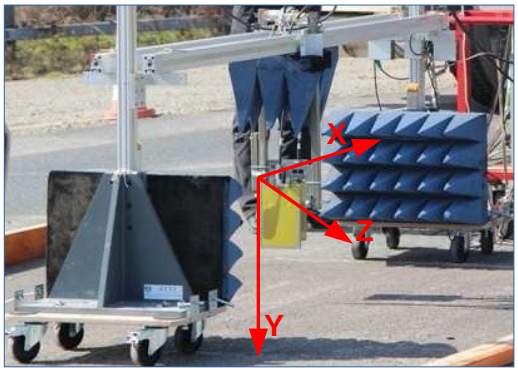

Figure 5: Experimental setup for data collection (surrounding blue cones are dampeners to avoid stray reflections) [27]

In Fig. 5, an automatic bench which is controlled by a computer can move the Tx and Rx antennas in both X (scanning direction) and Y axes (elevation). The scanning direction along the X-axis is about $150\,\mathrm{cm}$ at the most. The bench moves the antennas step-wise every $1\,\mathrm{cm}$ to $2\,\mathrm{cm}$ to collect data vectors, namely, A-scan profiles over the pavement. The set of vectors form a 2D B-scan image of the subsurface, as illustrated in Fig. 6. Dampeners on either sides on the Tx-Rx shield the receiver from the surrounding stray reflections from the bench.

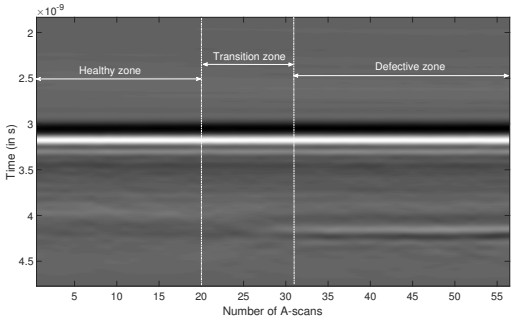

Figure 6: B-scan radargram of the subsurface (Experimental data: Tack-free at 10kcycles loading stage)

For the data collection, raw B-scan images were taken at each loading stage over each defective patch, each B-scan having 80 to 160 traces (A-scans) per image. B-scan images steps over small patches, namely for $[a, b, c]$ in Fig. 3. By contrast, two successive B-scans are required to collect the data over the largest patches, namely, for $[A, B, C]$ in Fig. 3. In the latter case, each B-scan were straddling between the two areas, namely, healthy *vs.* debonding, to ensure a visual control on data for e.g., as shown in Fig. 6. Finally, the free space antenna response is subtracted from the raw data to provide the radar signal to be analyzed and processed in the next section.

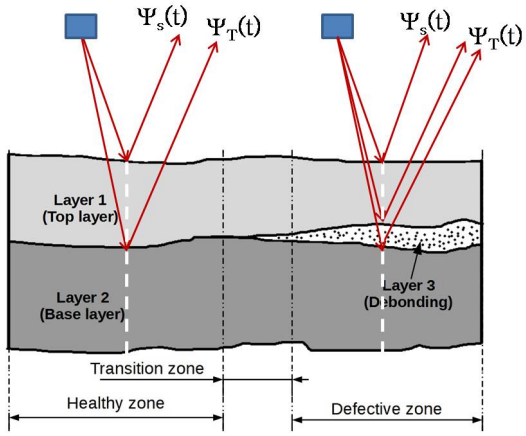

Figure 7: Pavement model showing healthy and defective regions. The transition zone refers to the section of the pavement whose condition cannot be determined

3. Debonding characterization

This section focuses on the way to characterize the interface condition between the first two layers of pavement structures from a material point of view at first and secondly, for the NDT techniques. Fig. 7 presents the pavement model with the defective zone, the healthy zone and the transition zone. The defective zone is the section of the pavement where the debonding is present in contrast to the healthy zone which is completely defect free due to the perfect coating between the two pavement layers. The transition between the two latter pavement structures may be smooth enough in practice to make difficult the decision whether a debonding is present or not.
Because pavement material is made of aggregates, the two sides of the debonding layer present rough interfaces. With time and wearing, interlayer stripping (erosion from the two adjacent layers) may occur; the debonding layer is thus made of a mixture of granular materials (of different sizes), air and also water. The permittivity is likely larger than the one of the two surrounding layers because of water seepage within the pavement structure. In this paper, the thickness of the debonding layer is supposed to be less than $\lambda_{mat}/4$ (where λ_{mat} is the wavelength in the debonding layer), namely, between a few millimeters to

one centimeter.

For NDT radar techniques, the healthy pavement structure gives rise to two reflected echoes: the first echo $\psi_S(t)$ is backscattered by the top surface of the pavement and the second one, $\psi_T(t)$, from the interface between the first and the second pavement layers. As the echo amplitude depends on the dielectric contrast at the interface, the first echo is the strongest whereas the second echo can be 10 times smaller assuming a small dielectric contrast between the two first layers as shown in Fig. 8.

The debonding pavement areas are assumed to appear as a thin-bed structure, *i.e.*, a sub-wavelength dielectric layer embedded between two dielectric layers with very similar permittivity values. Thin-bed structures have been extensively studied by EM and seismic NDT techniques, e.g., [28, 29, 30, 31].

When the EM signal impinges at the thin debonding layer, a several interference phenomena take place that alter both the amplitude and the phase of the EM signal [32, 33, 34]. As mentioned in [29], the reflection coefficient (and evidently, the amplitude) has a gradual increase upto $\lambda_{mat}/4$ limit after which, it decreases until $t_{deb} = \lambda_{mat}/2$ (where the two reflections are completely separated). This increase is due to the constructive interference (*i.e*, in-phase interference) between the reflected signal from the upper interface, the lower interface and the multiple reflection occurring within the debonding layer. The $t_{deb} = \lambda_{mat}/4$ is the maximum value at which the constructive interference takes place after which, the signals interfere destructively (*i.e*, out-of-phase interference).

According to Fig. 7, in defective zone, three echoes are expected. The two echoes which are reflected from the upper and the lower interfaces of the debonding overlap in time domain and mostly interfere constructively (since the thickness of the debonding layer is limited to be less than $\lambda_{mat}/4$ as mentioned in Section 2.1). The resulting composite echo $\psi_T(t)$ usually shows a larger signal strength and also a larger peak frequency compared to the echo over the healthy interface.

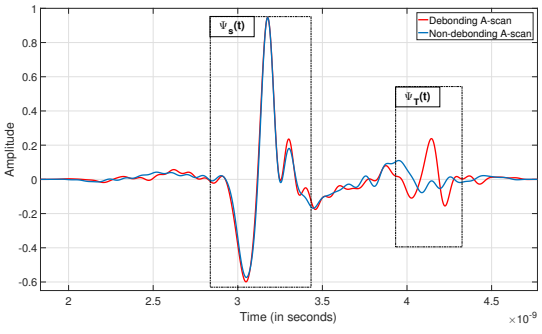

Figure 8: Comparison of A-scans for debonding and non-debonding cases (from Tack-free defect radargram at 10kcycles Fig. 6)

Fig. 8 presents two radar A-scans respectively for debonding and non-debonding cases (of Tack-free based defects at 10kcycles loading stage). The first echo comes from the top surface of the pavement which is the same for both cases. The second echo corresponds to the interface to survey. In case of debonding, the second reflection is characterized by a larger echo amplitude and an overall delayed reflection. For comparison, sand and geotextile defects (not shown here) would depict a stronger echo amplitude.

In the next section, the two data processing methods that are presented use certain signal characteristics such as the amplitude, delay and shape of the signal, to detect defective pavement sections.

4. Debonding detection methods

Different data processing techniques have been used to approach the subject of debonding. When the debonding is likely to be present in data, the first processing strategy would be to separate overlapping echoes by performing super time resolution processing techniques on the composite echo. Unfortunately, the best performance of the latter methods require the numbers echoes/interfaces to be known *a priori* [35].

In this section, an alternative processing strategy is used. Two processing techniques are presented to classify A-scan radar data into two classes, namely non-debonding (healthy) and debonding (defective) signal classes. ART is a conventional (unsupervised) reference method that uses the amplitude of the second echo as a signal feature to classify radar data [24]. Whereas SVM, on the other hand, is a supervised machine learning method which can use several signal features as input for achieving better performance [36].

4.1. Amplitude Ratio Test (ART)

ART is a conventional NDT method to detect subsurface delamination from GPR data [24, 27]. The ART method is usually carried out for qualitative diagnosis of pavement and bridge structures. It allows selecting the areas where some coring is performed to verify the NDT diagnosis. Although routinely used, ART method have not been extensively assessed from a statistical point of view. Any delamination/debonding provides additional echoes which mostly interact constructively with each other. This results in an increased signal strength of the backscattered signal that is received compared to the one of the healthy zone. In practice, the operator then searches for some increase in the interlayer echo magnitude along the radar scanning direction, namely, the second echo in our case. Besides, it is seen in [22] that larger amplitude increase can be achieved over the debonded area with the shorter

Tx pulses allowed by UWB stepped-frequency radar.
The ART values are usually computed for each A-scan data vector from the magnitude of both ψ_S and ψ_T echoes, as follows:

$$ART = \frac{max(|\psi_T(t)|)}{max(|\psi_S(t)|)} \tag{4.1}$$

Finally, the following normalized ratio is introduced for classification purpose:

$$ART_{norm} = \frac{ART_{test}}{ART_{ref}} \tag{4.2}$$

where ART_{test} is the ART value over the pavement area to test and ART_{ref} is the one for a reference data set over the healthy pavement structure. ART_{ref} may be theoretically computed as in [24] from the prior knowledge of the permittivity attached to the two first underlying layers, or experimentally established as in [22, 23]. For classification purpose, it comes for noiseless condition:

$$ART_{norm} = \begin{cases} = 1 \Rightarrow \text{Case Non-debonding (Healthy)} \\ > 1 \Rightarrow \text{Case Debonding (Defective)} \end{cases}$$

By contrast, the following definition of ART used in this paper is based on the measurement of the amplitude range of both ψ_S and ψ_T echoes for both healthy and debonded areas, as follows:

$$ART = \frac{|max(\psi_T(t)) - min(\psi_T(t))|}{|max(\psi_S(t)) - min(\psi_S(t))|} \tag{4.3}$$

Besides, taking advantage of the radar data base collected on the fatigue carousel, the decision threshold is established from the statistical distribution of the ART values over both healthy and defective areas. The Tack-free area is selected as the defective pavement structure because it leads to the smallest ART values compared to sand and geotextile defects.

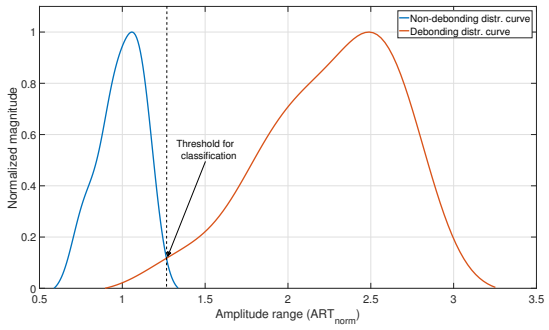

Figure 9: ART_{norm} PDF over Tack-free defect and healthy area at 10kcycles loading stage. The dashed vertical line depicts the decision threshold for debonding detection

For illustration, the Probability Density Function (PDF) of ART_{norm} values is plotted in Fig. 9. The decision threshold for classification is determined by finding the point of intersection of the two PDFs; it is found slightly above 1 owing to noisy conditions. Another explanation to this behavior could be due to the over-compaction of the pavement layers due to the traffic in the initial loading stages [11]. The decision threshold depends on the dielectric contrast between pavement layers but also on the interface roughness and the radar bandwidth.
Although ART is an easy-to-implement method, it only uses two signal features, *i.e.*, the amplitude range of both the surface and the interlayer echoes, namely, ψ_S and ψ_T. It is proposed in the next section to introduce a machine learning method, which uses several signal features as input instead, for expected better classification results.

4.2. Support Vector Machines (SVM)

Supervised learning is a type of machine learning where a set of data (training data) is used to produce model which can be used to map new data (test data) [37]. This scenario allows the algorithm to determine the classification for the unknown instances. Support Vector Machines (SVM) is one such machine learning algorithm.
The SVM we know today was first introduced by Boser, Guyon and Vapnik in the early 90s [38]. This was a non-linear generalization of Vapnik and Lerner's Generalized portrait algorithm introduced over fifty years ago [39] which was later extended by Vapnik for soft-margin and regression cases [36].

4.2.1. SVM for debonding detection

SVM is a classifier that can be used for binary classification. The aim of SVM is to find an optimal margin (also called as hyper-plane) from a set of different planes (Fig. 10b) that well separates the data-points of the two classes. The best separation is intuitively achieved with the hyper-plane which has the largest distance from the nearest data-points of the two classes (Fig. 10b) *i.e.* the hyper-plane that has the maximum margin between the two classes. Fig. 10a depicts the two classes of data and all possible hyper-planes separating the two classes while Fig. 10b shows the optimal hyper-plane.
The detection can be seen as a binary problem where +1 indicates the presence of a debonding layer whereas -1 indicates the absence of any such defects (*i.e.*, healthy region).
According to the literature, SVM can be formulated from either raw data samples or some signal features. In this section, let us define a vector $\mathbf{x}_i \in \mathbf{X}$ of length k. Here,

$\mathbf{X}$ is the time domain GPR B-scan under test with N A-scans and k is the number of features chosen from each A-scan. We define a vector $\mathbf{y} \in \{-1, +1\}$ which is the identifier vector.

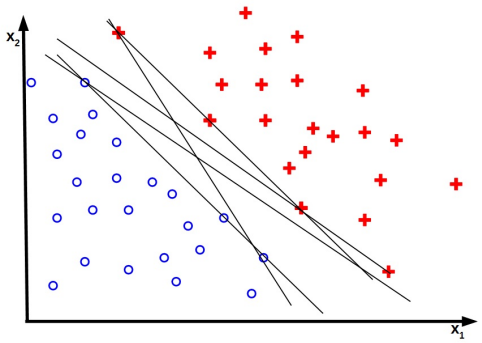

(a) All possible hyper-planes

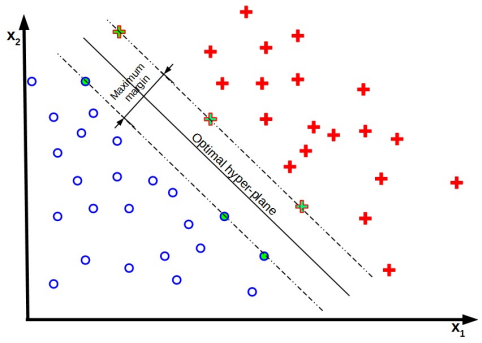

(b) Optimal hyper-plane for classification

Figure 10: SVM Hyper-planes. x_1 and x_2 are the the axes of the feature-planes

The separating hyper-plane is given by: $\mathbf{w}^T\mathbf{x} + b = 0$. So, we have the following cases:

$$\mathbf{w}^T\mathbf{x} + b > 0 \text{ if } y_i = +1$$
$$\mathbf{w}^T\mathbf{x} + b < 0 \text{ if } y_i = -1$$

Hence the decision function $D(\mathbf{x})$ is given by:

$$D(\mathbf{x}) = sgn(\mathbf{w}^T\mathbf{x} + b) \tag{4.4}$$

where $\mathbf{w}$ is the weight vector, $\mathbf{x}$ are the selected features of an A-scan and b is the bias.
The aim is to choose the best values for $\mathbf{w}$ and b such that the distance between the two classes is maximum. This problem can be written as follows:

$$\begin{aligned} \text{minimize} \quad & \frac{1}{2}\mathbf{w}^T\mathbf{w} + C\sum_{i=1}^{N}\xi_i \\ \text{subject to} \quad & y_i(\mathbf{w}^T\mathbf{x}_i + b) \geq 1 - \xi_i, \\ & \xi_i \geq 0, i = 1, 2, ...N. \end{aligned}$$

where, ξ_i is the slack variable introduced to reducing training errors and C is the regularization parameter. The decision function can now be written as:

$$D(\mathbf{x}) = sgn(\sum_i \mathbf{w}^T\alpha_i\langle\mathbf{x}_i, \mathbf{x}\rangle + b) \tag{4.5}$$

where α_i are the Lagrangian multipliers and $\langle ., . \rangle$ is the dot product.
However, in some cases, the data cannot be separated linearly. Thus, a kernel trick is used. In such cases, the data is mapped onto a higher dimensional space $\mathcal{H}$ using the function $\phi(.,.)$ through dot products $\langle ., . \rangle$. The solution for non-linear SVM is thus given by:

$$D(\mathbf{x}) = sgn(\sum_i \mathbf{w}^T\alpha_i\Phi(\mathbf{x}_i, \mathbf{x}) + b) \tag{4.6}$$

where $\Phi(\dots)$ is the kernel function.
There are several kernel functions in SVM some of which include polynomial kernel, sigmoid kernel, radial basis function *etc.* [40]. In this paper, we use the Radial basis function (RBF) kernel.

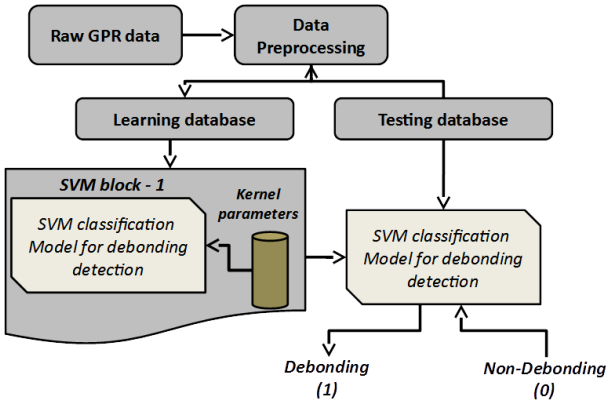

Figure 11: Flowchart depicting the working principle of SVM to detect debondings

The application of SVM to detect debondings is depicted in the flowchart in Fig. 11. Certain signal characteristics are extracted from the raw GPR data in the first step. Then SVM is performed on said features (local or global).

4.2.2. Avoiding overfitting

One of the major problems encountered in machine learning is the concept of over-fitting. Over-fitting is generally associated to the oversampling of data. To avoid this, various methods such as as regularization, ensembling, early-stopping, leave-out, hold out, cross-validation *etc*. have been discussed in the literature. Indeed, cross validation (CV) can also be used in this context; to simply identify over-fitting [41]. So, in this paper, we use CV to do it.

To detect the over-fitting, we use CV constrained by the root-mean square error of positive identification. The learning dataset is initially divided into $k = 5$ equal folds. Then, the classification method is used with the optimal hyper-parameters obtained with CV and on both training and validation databases. The behavior of the classification method from both databases allow to determine the presence of over-fitting.

4.3. Signal features selection

Most GPR data are very large containing thousands of time samples. From this huge data set, it is possible that a part of the data is redundant and presents negligible or no information at all. In the machine learning classification problems, the first step is then to perform data reduction by identifying and selecting the data subset that provides maximum information.

Feature extraction refers to obtaining such relevant information that can be useful to classify the data [42]. As mentioned in [43], features should be able to distinguish between the two classes, efficient in computations, limited in number and also insensitive to the changes in the data. The advantages of using features is that they reduce the computational time, possible increase in the accuracy [44] and also avoid using redundant data [45].

For our application, we broadly classify the signal features as either temporal (time-domain) features or spectral (frequency domain) features. Temporal features of the signal are selected in this paper as they are easy to implement and require no transformation.

Additionally, the temporal features are sub-categorized into local and global features. Local features are defined as the characteristics extracted from the second echo of the raw GPR A-scan. Global features on the other hand are defined as the signal characteristics that are obtained from the complete raw GPR A-scan. Global features are advantageous as they are easier extract and require minimal preprocessing and *a priori* information, as opposed to the local features. In case of GPR data, global features are usually dominated by the surface clutter and are therefore supposed to be less sensitive to the debonding. Whereas local features are expected to provide more sensitive information about the interface between the first two pavement layers and the debonding that may occur therein.

The two next subsections introduce both local and global temporal features of the signal which have been used for performing SVM classification. The feature selection presented later in Section. 4.3.3 relies on the prior knowledge about the fatigue carousel data base.

4.3.1. Local features

Local features are expected to provide more sensitive information about the interlayer pavement conditions. They are defined as the signal characteristics of the original raw GPR A-scan over a short time window, whose center and duration are computed from the data for each A-scan. The window is centered on the second echo (which is supposed to be related to the debonding interface) from time picking of the magnitude, and its time duration Win_{TG} (in samples) is given as:

$$W_{TG} = f_{samp} \times t_{width} \tag{4.7}$$

$$Win_{TG} = 2 \times W_{TG} \tag{4.8}$$

where f_{samp} is the sampling frequency (in Hz) and t_{width} is the emitted ricker pulse width (in seconds), which is related to the central pulse frequency.

A Tukey cosine-tapering window [46] with a taper ratio of 25% is used to select the time-gated samples attached to the interlayer echo, as shown in Fig. 12. The taper ratio is fixed in such a way that the unwanted noise and parasitic signal around the second echo is avoided and at the same time the important information is preserved.

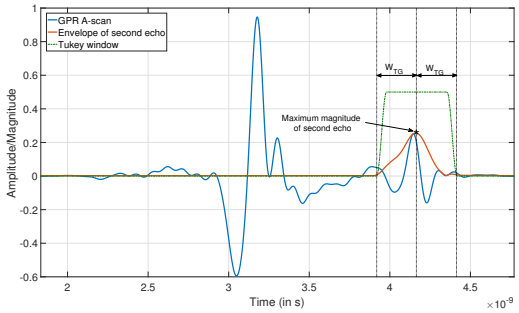

Figure 12: Example of the time-gating window for an experiment GPR trace (Debonding Tack-free defects at 10kcycles)

Three kinds of local feature subsets have been selected from the literature, namely, Statistical, Morphological and PQRST features. As in [47, 48, 49], local statistical features used here are: Standard deviation, Mean absolute deviation (MAD), Kurtosis and Skewness. Morphological features have been introduced to account for the shape of the echo; Inter-quartile range and Root-mean square

(RMS) of the local signal are then also used [50].

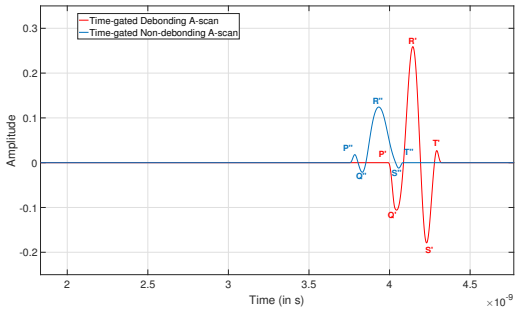

Figure 13: Comparison of PQRST features for debonding and non-debonding cases (computed from Tack-free defect radargram at 10kcycles Fig. 6). [P', Q', R', S', T'] and [P", Q", R", S", T"] respectively represent the PQRST features for debonding and non-debonding cases

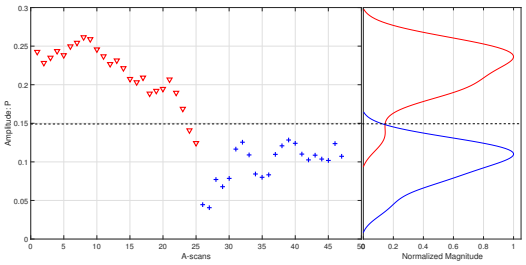

(a) Amplitude at point P

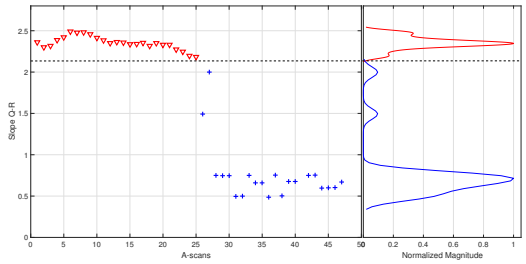

(b) Slope Q-R

Figure 14: Physical representation of PQRST features for experimental data (computed from Tack-free defect radargram at 10kcycles Fig. 6). '▽' indicate debonding and '+' indicate non-debonding values

Additionally, specific Electrocardiography (ECG) signal features have been used due to the similarity between the GPR A-scan and an ECG signal, namely the PQRST features discussed in [51, 52]. Fig. 13 shows the PQRST data-points in a GPR signal for debonding and non-debonding for the second echo. The selected PQRST features in our application are the slope QR and the amplitude at points P and T. Fig. 14a and 14b depict some of these features.

The constructive interference of the reflections within the debonding layer results in an observable increase in the characteristics of the second reflection such as amplitude range. Fig. 15 shows an example of the difference between the reflections of debonding and non-debonding case. Thus, amplitude range and magnitude of the second echo are used as local features. These are grouped under the Morphological feature subset.

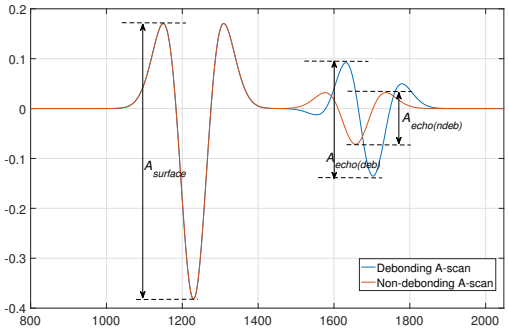

Figure 15: Comparison of amplitude range for debonding and non-debonding cases (from 1D simulated model)

4.3.2. Global features

Global signal features are defined as the signal characteristics that are obtained from the raw GPR A-scan. These features are relatively easier to extract compared to the local features as they use the complete A-scan. Additionally, these features do not require any information *a priori* as is the case for local features.

In this paper, the global statistical features of MAD, Standard deviation, Skewness and kurtosis are used. Additional features such as RMS of a signal and the Interquartile range are also used. Table. 1 sums up the local and global features that will be used in this paper.

4.3.3. Feature selection process

The performance of a machine learning method depends on the hyper-parameters, kernel function and also the choice of its input data [53]. As such, a lot of effort is required to design the preprocessing steps for data transformation and feature extraction [53]. This initial process is called Feature engineering.

Methods such as Principal Component Analysis [54], feature weighting [55] and Recursive Feature Elimination [56] have been studied in the literature that perform automatic selection of signal features. These methods tend to limit either interacting or redundant signal features to represent data.

As opposed to the latter, we take advantage of the ground truth associated to the data base (see Section. 4.4 hereafter) to perform the feature selection. The ground truth categorizes the A-scans into two classes, namely

Time domain signal features
1. **Local features**:
• Statistical features: *MAD*, *Std. deviation*, *Skewness*, *Kurtosis*
• Morphological features: *RMS of the signal*, *Inter-quartile range*, *Amplitude and Magnitude of second echo*
• PQRST features: *Amplitudes P and T*, *Slope QR*
2. **Global features**:
• Statistical features: *MAD*, *Std. deviation*, *Skewness*, *Kurtosis*
• Morphological features: *RMS of the signal*, *Inter-quartile range*

Table 1: Concise list of the local and global features used.

debonding and non-debonding cases. The probability density function (PDF) of the features (listed in Table. 1) is computed over each class to determine those which are sensitive enough to the pavement conditions.

Initially, a known B-scan with debonding and non-debonding regions is taken. PDFs are traced for each feature listed in Table. 1 for debonding and non-debonding cases. Fig. 16 and Fig. 17 present some of the features to indicate how each feature is able to distinguish between debonding and non-debonding cases. For representation only, a curve-smoothing technique using moving average is applied to the PDFs in Fig. 16 and Fig. 17.

The separation between the two curves is used to choose the best features for our application. For example, the mean of the signal (represented in Fig. 16a, Fig. 17a) show minimal/no PDF separation whereas standard deviation (Fig. 16c, Fig. 17c), Kurtosis (Fig. 16d, Fig. 17d) and Skewness (Fig. 16e, Fig. 17e) provide well-separated PDFs. Thus the mean is rejected whilst the other features are used.

4.4. Pseudo-ground truth estimation

The performance of the data processing methods in Section. 5 relies on a reference benchmark dataset, which is detailed in this section. The latter benchmark dataset is called Ground Truth (GT) when the operator has full information about the spatial distribution of debondings. Otherwise, Pseudo Ground Truth (PGT) is used instead when the operator infers the spatial location of debondings from *in situ* measurements. The generated PGT is a binary vector consisting of '1' (to indicate debonding) and '0' (to indicate non-debonding).

For the experiment data collected using SFR at the carousel, the operator manually creates the PGT vector from radar B-scan images, for which debonding and non-debonding are labeled by '1' and '0', respectively. The debonding area is visually easy to locate owing to the larger magnitude of the second echo, as illustrated in Fig. 18. The stationary properties of the B-scan images in both the time and the frequency domains helps the operator to divide the GPR images into 3 parts: the defective zone, the healthy (non-debonding) zone and the transition zone. The transition zone corresponds to the edge effect which is induced by the implementation of pavement materials; the stratified structure is then not so steady defined compared to the two zones apart. The data processing methods ignore the transition zone within the GPR image during the detection process. Fig. 18 presents an example of the PGT associated to the B-can recorded over the tack-free area. In this PGT, the labels '1' and '0' respectively represent debonding and non-debonding.

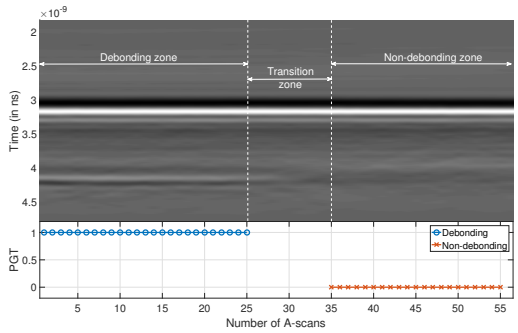

Figure 18: PGT proposed by the operator for a GPR image: Tack-free defects at 10kcycles loading stage. PGT is not estimated for the Transition zone

4.5. Performance evaluation

For each B-scan image, the classification result is compared to the PGT. There are four possible outcomes namely, False positive (FP or false alarm), False negative (FN or undetected debondings), True positive (TP or good detection) and True negatives (TN or no debonding), as shown in Fig. 19.

The three first categories, *i.e.*, TP, FP and FN, are used to

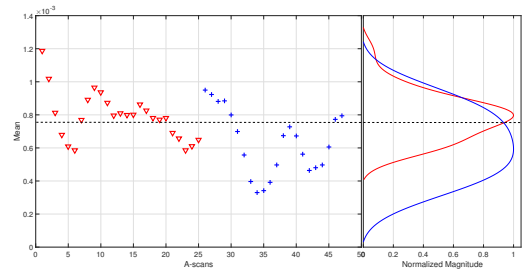

(a) Mean

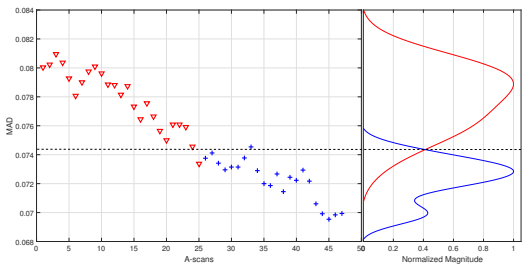

(b) Mean absolute deviation (MAD)

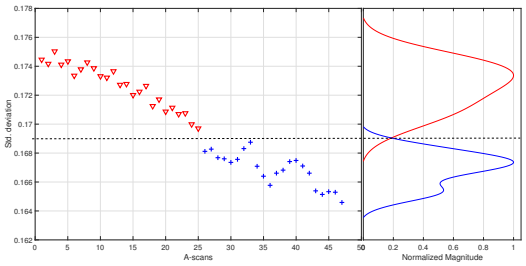

(c) Standard deviation

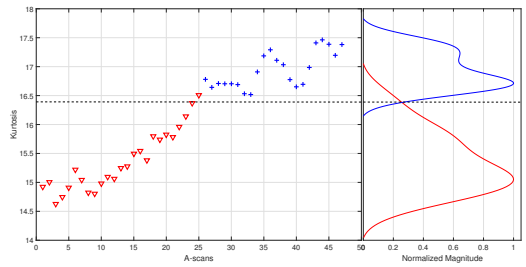

(d) Kurtosis

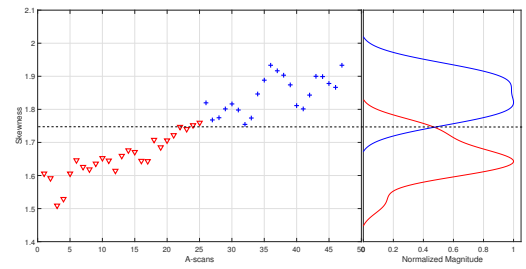

(e) Skewness

Figure 16: Physical representation of global features for experiment data (computed from Tack-free defect radargram at 10kcycles Fig. 6). '▽' indicate debonding and '+' indicate non-debonding values

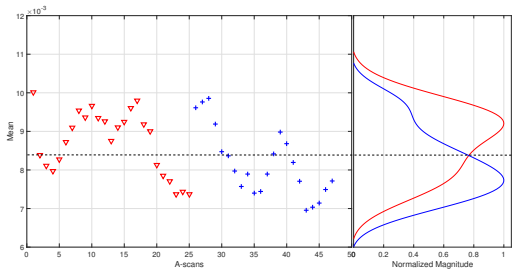

(a) Mean

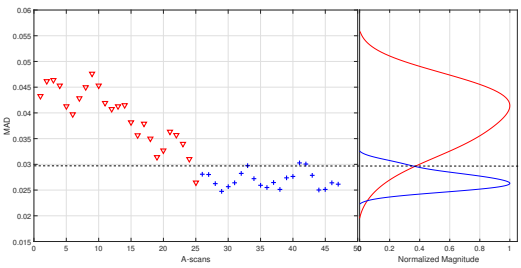

(b) Mean absolute deviation (MAD)

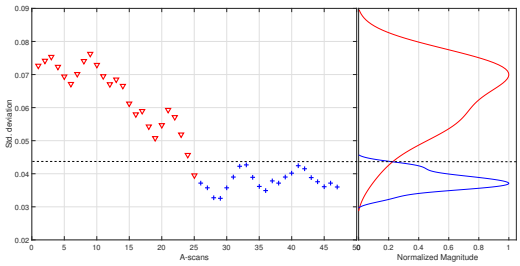

(c) Standard deviation

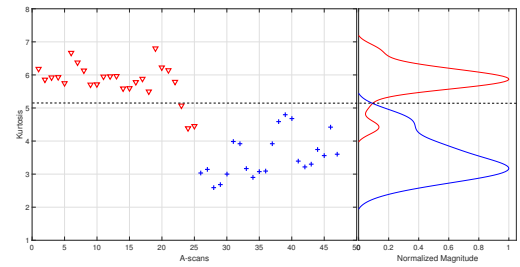

(d) Kurtosis

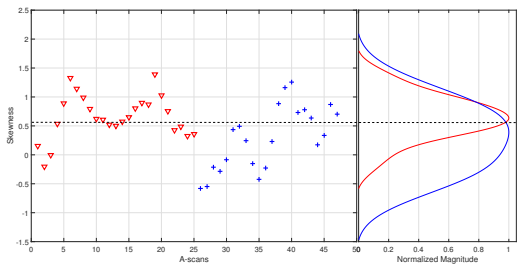

(e) Skewness

Figure 17: Physical representation of local features for experiment data (computed from Tack-free defect radargram at 10kcycles Fig. 6). '▽' indicate debonding and '+' indicate non-debonding values

compute the Precision (P) and the Sensitivity (S or Recall) which indicates the rates of false alarm and the rate of undetected debondings, respectively. Finally, the harmonic mean of P and S coefficients [10] is used to evaluate the performance of the detection methods; it is called the Dice coefficient (DSC) or the F1-score, equivalently [57]. The DSC can be written as:

$$DSC = \left(\frac{1}{2}\left\{\frac{1}{P} + \frac{1}{S}\right\}\right)^{-1} \tag{4.9}$$

where P and S are respectively given by [10]:

$$P = \frac{TP}{TP + FP} \tag{4.10}$$

$$S = \frac{TP}{TP + FN} \tag{4.11}$$

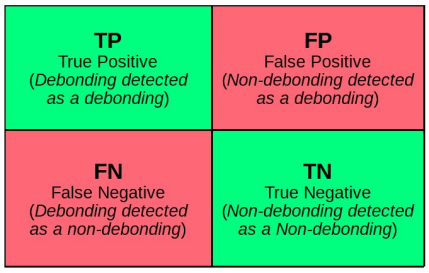

Figure 19: Confusion matrix for debonding detection

In practice, the three criteria are 1 if the two classification results are perfectly matched to each other, and 0 if there is no superposition. A large difference between the S and P coefficients strongly impacts the DSC rate. Within the image processing community, the classification result is usually considered as good enough for DSC values ≥ 0.7 [57].

5. Results

The classification results obtained by the conventional reference method (ART) and Supervised machine learning method (SVM) are presented in Sections. 5.1 and 5.2, respectively and compared to each other as mentioned in Fig. 20. ART is a conventional debonding detection approach that was developed in MATLAB®. SVM was implemented using the well-known LIBSVM [40] library in MATLAB®.
The selected strategy has been to optimize the methods for each type of defects separately, namely, tack-free, sand and geotextile. The two formulations of the SVM method shown in Fig. 20, *i.e.*, from raw data samples and from either global or local signal features, are used to perform sensitivity analysis of SVM later in Section. 5.3.

The performance of methods are evaluated using DSC similarity index, S and P rates as mentioned in Section. 4.5.

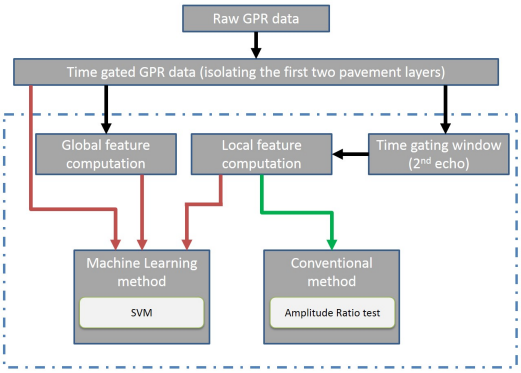

Figure 20: Overview of debonding detection approach by ART and SVM

5.1. ART detection results

For ART, the 10kcycles loading stage has been selected as training data. The ratio ART_{norm} is calculated and a threshold is chosen for each type of defect at 10kcycles. The obtained values are respectively $\eta_{geo} = 1.9$, $\eta_{sand} = 1.49$ and $\eta_{tf} = 1.34$ for Geotextile, Sand and Tack-free. These threshold values are then used to classify the defective zones for the remaining loading stages (*i.e.* 50k, 100k and 200k, 250k and 300kcycles).
Fig. 21a presents the DSC score for ART at each loading stage for Geotextile, Sand and Tack-free based defects. It can be seen that the detection is consistent for Sand and Geotextile defects due to the good PDF separation. However for Tack-free, false detection reduce the detection rate. These false detection could be attributed to the fact that PDFs over Tack-free and healthy areas shows a larger overlapping compared to the Sand and Geotextile areas.
However, it should be noted that, in real-time scenarios, the type of defect is not always known. Hence, using a defect-independent global threshold (η_{global}) is more practically suitable. Thus, the global threshold to be selected to this aim is the smallest one among the three defect types at 10kcycles loading stage, $\eta_{global} = 1.34$ for Tack-free. This threshold is used over the subsequent data (each defect type over various loading stages) to detect debondings. Fig. 22 compares the DSC score for the three defects obtained using η_{global} and the individual thresholds (*i.e.* η_{geo}, η_{sand} and η_{tf}). It can be observed that the false detection in Geotextile and Sand based defects increase due to the difference in the thresholds.

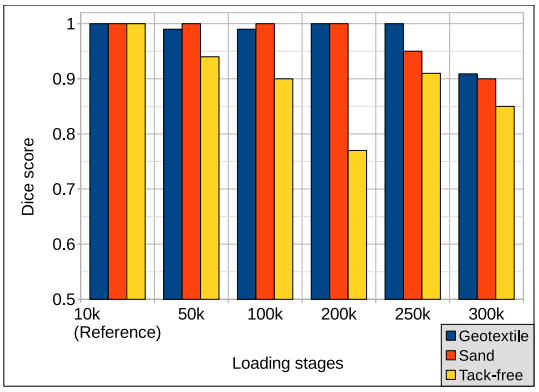

(a) ART using ART_{norm} as signal feature

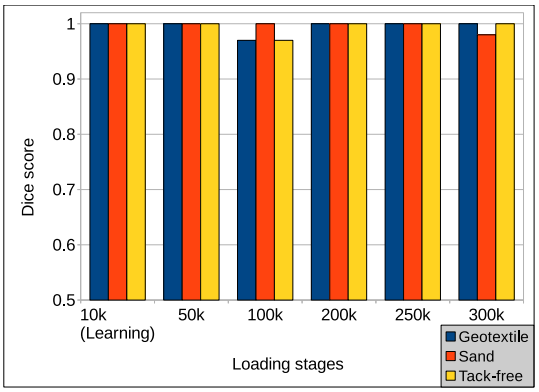

(b) SVM using the time-gated raw GPR signal

Figure 21: DSC score for all defect types at all loading stages. For ART, 10kcycles (reference) is used to obtain the threshold for each defect type; for SVM, 10kcycles is used as learning data for each defect type

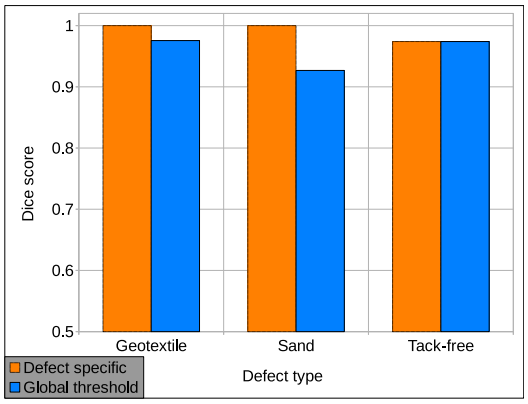

Figure 22: Comparison of DSC score for all defects at 100kcycles using $\eta_{geo} = 1.9$, $\eta_{sand} = 1.49$, $\eta_{tf} = 1.34$ *vs.* $\eta_{global} = \eta_{tf} = 1.34$

5.2. SVM detection results

This subsection presents the classification results of the straightforward application of SVM on raw GPR B-scan data, as mentioned in Fig. 20. As in [10], the RBF kernel is used with hyper-parameters C and γ. The optimal values for C and γ are obtained by grid-search cross validation as described in [58]. For Geotextile, sand and tack-free defects, the hyper-parameters are presented in Table. 2. Here, the 10kcycles loading stage is used as training data to generate a classification model. This model is then used to classify the test data (*i.e.* the subsequent loading stages).

Data type	Raw GPR data
Geotextile	$C = 500, \gamma = 0.2$
Sand	$C = 840, \gamma = 0.025$
Tack-free	$C = 600, \gamma = 0.025$

Table 2: List of optimal input parameters used in LIBSVM for RBF kernel on raw GPR data

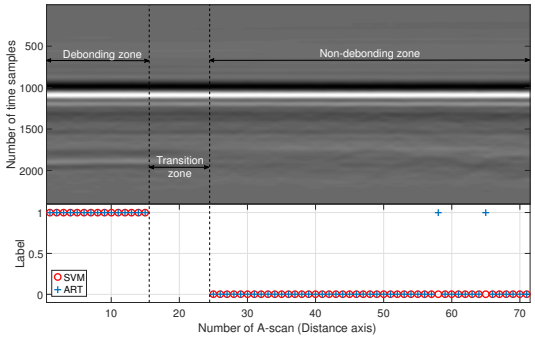

(a) 50kcycles

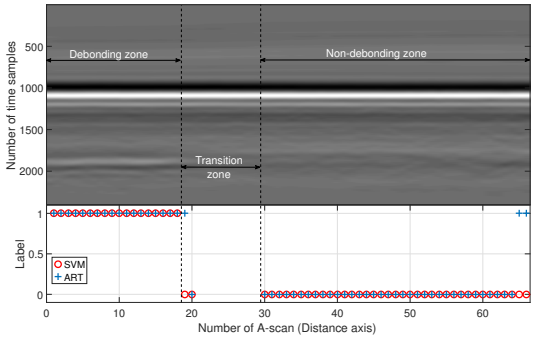

(b) 100kcycles

Figure 23: ART and SVM detection for Tack-free defects. SVM results are obtained using the time-gated raw GPR signal (*i.e.* no signal features used)

Fig. 23a and Fig. 23b compare the detection by ART and SVM for Tack-free defects at 50k and 100kcycles loading stages.

Fig. 21b presents the DSC score SVM at each loading stage. It is observed that SVM provided an improved detection rate over the conventional ART method with excellent detection in case of Geotextile defects while very

few false detection in case of Sand and Tack-free defects. As mentioned in Section. 4.3, the use of suitable signal features could possibly improve the results. Thus, in the next section, the detection results using SVM are presented where we analyze the performance of SVM *w.r.t.* various sensitivity parameters.

5.3. SVM Sensitivity analysis

Various sensitivity analysis (SA) of SVM have been discussed in the literature, e.g., [44, 59, 60, 61]. Within the scope of the application, the objective of SA is twofold. This is first, to identify the formulation of SVM, which achieves the best efficiency and robustness. The second objective aims at identifying the parameters that control the performance of the methods.
In this section, we broadly classify SA into the two following parts. Parameter-based SA refers to the analysis based on the input parameters (i.e. the signal features *etc.*). On the other hand, model-based SA is the analysis of SVM behavior *w.r.t.* the model parameters (such as kernel parameters, training to test ratio *etc.*).

5.3.1. Parameter-based sensitivity analysis

The time-domain global and local signal features introduced in Section. 4.3 are selected to perform SVM on GPR data. The classification results are compared to each other and to the results shown on Fig. 21b. In addition to that, the results are compared to a well-known automatic feature extraction method namely, principal component analysis (PCA). PCA has been used with SVM to classify Electroencephalography (EEG) signals [62], ECG signals [63] and pattern identification [64].
In this paper, PCA is performed separately on local and global feature sets. It was observed that, at first, the whole set of PCA features (*i.e.* at 100% PC inertia) allows us to achieve the same performance as for the original feature set. The inertia was brought down to 90% and similar performance levels were observed. However at 90% PC inertia, the use of PCA is unnecessary for both, the scope of the application and the feature set as since there is hardly any data reduction.
On further reducing the PC inertia, it was observed that the DSC score drastically drops for a PC inertia below 80% ($DSC < 0.5$). This is illustrated later in Fig. 25. In this section, an inertia of 80% (which results in 8 and 5 principal components for local and global features, respectively), is used.
As done in Section. 5.2, the Gaussian RBF kernel is used along with cross-validation during the training stage. The hyper-parameters are obtained by cross-validation and grid-search. Table. 3 presents the various hyper-parameters obtained using CV-Grid search for each feature subset and were used on Test data.

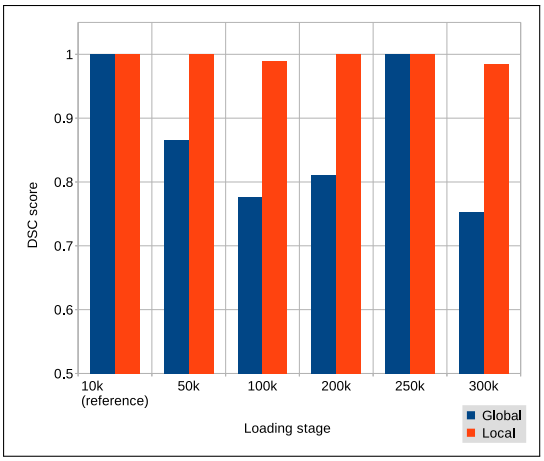

Figure 24: DSC score *vs.* Loading stage for Global and local feature sets for Sand based defects

Data type	Optimal hyper-parameters
Local features	$C = 900, \gamma = 0.08$
Global features	$C = 840, \gamma = 0.025$
PCA (Local features)	$C = 500, \gamma = 0.2$
PCA (Global features)	$C = 800, \gamma = 0.02$

Table 3: List of optimal input parameters used in LIBSVM for RBF kernel on various feature sets for Tack-free defects

As discussed in Section 4.3.1, the local features are expected to provide better classification results than global features since they are more sensitive to the interface under survey.This was further verified by the authors on various simulated data models (Fresnel-based analytic model and FDTD-based numerical model). Experimentally, the Sand based-defects and Geotextile-based defects support the claim. For convenience, this is only illustrated in Fig. 24) over the sand-based defect.
However, this behavior is not fully verified for Tack-free data, for which the debonding echo presents the weakest SNR. The best classification results for tack-free defects were achieved with global features over the debonding area (as presented in Fig. 25).
For this case, the classification results is assumed to be more sensitive to the "quality" of the reference data over the debonding area. And indeed, the quality of the echo is not as good as expected since the SNR of the echo over the non-debonding area is very small and disturbed by various wave scattering phenomena (including the interface roughness).
As a result, the back-scattered echo does not look like as the expected attenuated and delayed copy of the surface echo but as the sum of small echoes scattered over a

larger time interval.

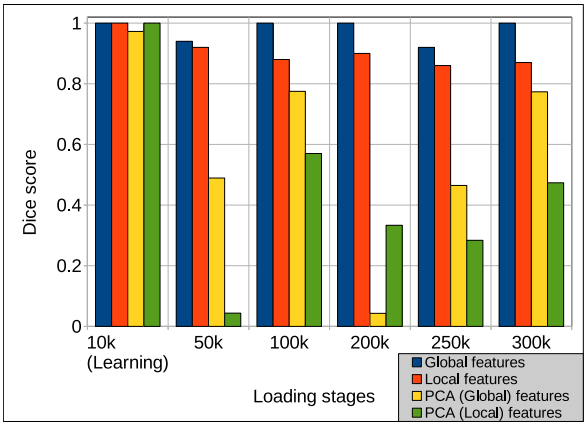

Figure 25: DSC score for SVM SA with various input feature sets (Tack-free defects): PCA features (local and global), Local features (Section. 4.3.1) and Global features (Section. 4.3.2); SVM results using raw data samples are shown in Fig. 21b

The second parameter based SA is a derivative of the one-at-a-time (OAT) [65] approach. This refers to the performance analysis of a method by using just one feature at a time. Here we perform the OAT approach for the local features due to the diverse nature of feature subsets under local features (Table. 1). [66] monitors the performance of SVM by varying the number of features in the training dataset. However, in the feature subset-OAT, we analyze the performance of SVM *w.r.t.* each subset.

As mentioned in Section. 4.3, two feature types namely local and global time domain features are used in this article. Under local features, we have the statistical, PQRST and Morphological feature subsets (as indicated in Table. 1). The OAT SA will be carried out on these local feature subsets in an attempt to improve the detection rate using local features (if possible). The performance with each subset presents the 'weight' the subset carries for efficient detection. If a subset presents improved results, the said subset has a greater impact on the performance. As done in Section. 5.2, the SVM RBF kernel with cross-validation is used. Table. 4 presents the various hyper-parameters obtained using CV-Grid search and were used on Test data.

Fig. 26 shows the variation in DSC score for each local feature subset. The figure presents the DSC score for Tack-free defects as these defects are difficult to detect and are the closest to the realistic pavement defects. It is seen that the individual feature subsets have a better performance compared to the complete local feature set (*i.e.* combination of statistical, morphological and PQSRT subsets). The Morphological feature subset presented the best results. Additionally, no change in the detection rate was observed to the order of the feature subset.

Data type	Optimal hyper-parameters
Local features	$C = 900, \gamma = 0.08$
Statistical features	$C = 500, \gamma = 0.2$
PQRST features	$C = 615, \gamma = 0.6$
Morphological features	$C = 2148, \gamma = 0.815$

Table 4: List of optimal input parameters used in LIBSVM for OAT approach using RBF kernel for Tack-free defects

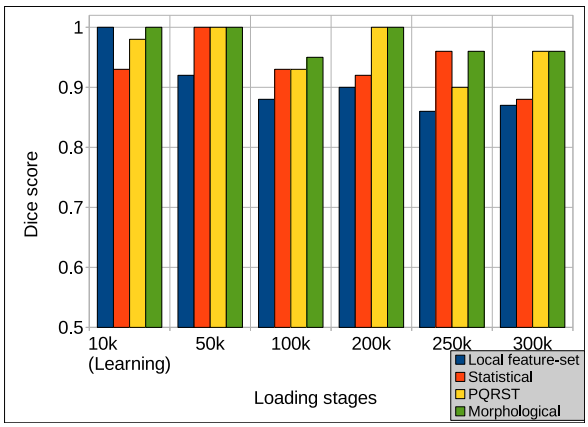

Figure 26: DSC score for SVM SA by Feature OAT subset approach for Tack-free defects at all loading stages using local signal features (Section. 4.3.1)

5.3.2. *Model-based sensitivity analysis*

For classification applications, SVM can use various mathematical functions called '*kernels*'. As discussed in Section. 4.2, a linear kernel is used for linearly separable data whereas for non-linearly separable data, there are various kernels. Some of the non-linear SVM kernels include: Gaussian RBF, Sigmoid, Polynomial kernel, *etc*. Each kernel is implemented using the LIBSVM [40] library.

Here, we analyze the SVM performance for various kernels (as done in [67] for classification of Landsat and QuickBird datasets and [68] for diagnosis of respiratory diseases). Each iteration implements a kernel type for the local feature set (defined in Section. 4.3.1). Fig. 27 shows the SVM performance with each of the kernels for Tack-free defects. The training to test ratio used was 50% : 50%. It is seen that for Tack-free defect type, the Gaussian RBF kernel presented an overall improved performance over other kernels. The optimal hyper-parameters used for each kernel function are as mentioned in Table. 5.

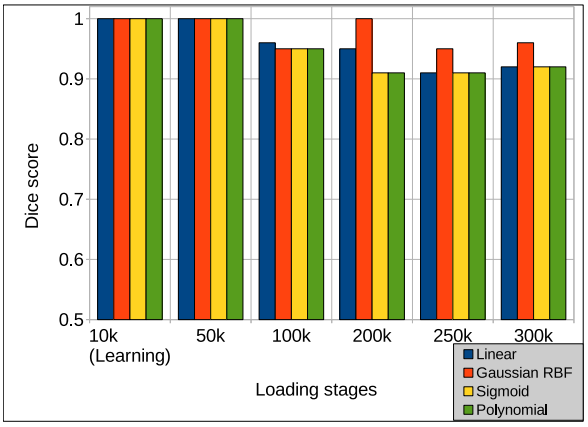

Figure 27: DSC score for SVM SA with linear, RBF, sigmoid and polynomial kernels at all loading stages for Tack-free defects using local features (Section. 4.3.1)

Data type	Optimal hyper-parameters
Linear	$C = 840$
RBF	$C = 900, \gamma = 0.08$
Sigmoid	$C = 900, \gamma = 0.08, coef_0 = 0$
Polynomial	$C = 900, \gamma = 0.08, degree = 3$

Table 5: List of optimal input parameters used in LIBSVM [40] for kernel Sensitivity analysis for Tack-free defects

Since SVM uses a small part of the data for training, their sensitivity to space dimensionality is very low [44]. However, the overall detection efficiency is susceptible to the number of training samples [69]. By using very few training samples, there may be the problem of under-fitting leading to a low performance rate. On the other hand, a very large number of training samples may lead to over-training which once again reduces the performance. Hence it is necessary to utilize an optimal training to testing samples ratio.

We therefore analyze the SVM sensitivity *w.r.t.* various training dataset sizes. The ratio of Training data *w.r.t.* Test data is varied and the performance is evaluated. The global feature set (discussed in Section. 4.3.2) along with a Gaussian RBF kernel is used here.

Fig. 28b plots the variation in DSC score *w.r.t.* the training dataset size at 50k, 100k and 300k cycles loading stages for Tack-free based defects using the global feature set (discussed in Section. 4.3.2). From Fig. 28b and Fig. 28a, it can be seen that for small training data sets, the debonding detection rate is low. Additionally, for these datasets, if the training data set is too large, the performance is once again reduced. An optimum data set size for training step is as indicated in Fig. 28b and Fig. 28a (*i.e.* between $\approx 50\%$ to $\approx 80\%$) for both local and global feature sets. These results are in accordance with the conclusions of $m_{train} \approx 66\%$ (as in [70]), $m_{train} = 70\%$ (as in [71, 72]), $m_{train} = 75\%$ (as in [73]) and $m_{train} = 75\%$ (as in [74]), all where m_{train} is the percentage of training data set *w.r.t.* test data set.

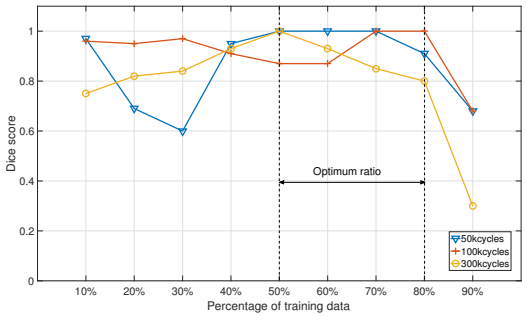

(a) Local feature set

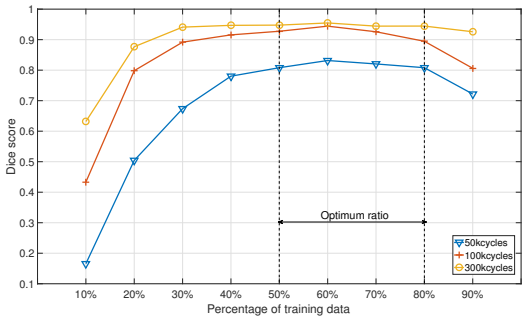

(b) Global feature set

Figure 28: DSC score at various Training sizes for SVM SA for Tack-free defects at 50k, 100k and 300kcycles loading stages. The vertical dashed line indicates the optimum ratio to obtain the best detection rate

Fig. 28a plots the variation in DSC score *w.r.t.* the training dataset size at 50k, 100k and 300k cycles loading stages for Tack-free based defects using the local feature set (discussed in Section. 4.3.1). In both cases, the RBF kernel is used.

6. Conclusions and Perspectives

The objectives of this paper was to detect the presence of horizontally stratified debondings between the top two layers of the pavement structure and monitor their growth over time. To do so, two methods namely, ART and SVM were used. Each method was used to monitor the pavement degradation over time by detecting debondings over various loading stages for various defect types. ART was implemented using a single signal characteristic whereas

SVM implemented several different features in time domain.

From the initial results, it was observed that SVM was highly efficient to detect debondings. To observe the robustness of SVM, sensitivity analysis was carried out by various Parameter and Model-based approaches. It was observed that SVM was successfully able to detect both strong (Geotextile) and weak (Tack-free) debondings with greater accuracy. These results showed the robustness of SVM method and its effectiveness in the detection process.

In this article, we concentrated on the use of certain temporal features. In perspective, this work can be further extended to include other temporal features and spectral features to further augment the results. Additionally, the research can be extended to detect the type of defect. We also look forward to measure the thickness of debondings.

References

[1] J.-F. Corté, M.-T. Goux, Design of pavement structures: The french technical guide, Transportation Research Record 1539 (1) (1996) 116–124. doi:10.1177/0361198196153900116.

[2] S. Chea, Contribution à l'auscultation structurelle des chaussées mixtes: Détection de défauts d'interface à l'aide de la déflexion, Ph.D. thesis, PhD. Thesis, in French, INSA de Rennes (2007).

[3] A. Benedetto, F. Tosti, L. B. Ciampoli, F. D'Amico, An overview of ground-penetrating radar signal processing techniques for road inspections, Signal Processing 132 (2017) 201 – 209. doi:10.1016/j.sigpro.2016.05.016.

[4] Y. Jimoh, I. O. Itiola, A. Afolabi, Destructive and non-destructive determination of resilient modulus of hot mix asphalt under different environmental conditions, International Journal of Pavement Engineering 16 (10) (2015) 857–867. doi:10.1080/10298436.2014.964235.

[5] R. A. Livingston, Nondestructive testing of historic structures, Archives and Museum Informatics 13 (3) (1999) 249–271. doi:10.1023/A:1012416309607.

[6] X. Wang, Q. Guo, S. Yang, D. Zhang, Y. Wang, Nondestructive testing and assessment of consolidation effects of earthen sites, Journal of Rock Mechanics and Geotechnical Engineering 8 (5) (2016) 726 – 733. doi:10.1016/j.jrmge.2016.06.001.

[7] M. Andrzej, M. Marta, Modern ndt systems for structural integrity examination of concrete bridge structures, Procedia Engineering 91 (2014) 418 – 423, xXIII R-S-P Seminar, Theoretical Foundation of Civil Engineering (23RSP) (TFoCE 2014). doi:10.1016/j.proeng.2014.12.086.

[8] B. Hankes, D. Couse, Condition monitoring and non-destructive testing of mechanical equipment, in: 2007 IEEE Cement Industry Technical Conference Record, 2007, pp. 160–167. doi:10.1109/CITCON.2007.358995.

[9] W. W. Lai, X. Dérobert, P. Annan, A review of ground penetrating radar application in civil engineering: A 30-year journey from locating and testing to imaging and diagnosis, NDT & E Internationaldoi:10.1016/j.ndteint.2017.04.002.

[10] S. S. Todkar, C. L. Bastard, A. Ihamouten, V. Baltazart, X. Dérobert, C. Fauchard, D. Guilbert, F. Bosc, Detection of debondings with ground penetrating radar using a machine learning method, in: 2017 9th International Workshop on Advanced Ground Penetrating Radar (IWAGPR), 2017, pp. 1–6. doi:10.1109/IWAGPR.2017.7996056.

[11] J.-M. Simonin, V. Baltazart, C. Le Bastard, C. A. Dérobert, X., W. G. Buttlar, E. V. Dave, C. Petit, G. Tebaldi, Progress in monitoring the debonding within pavement structures during accelerated pavement testing on the fatigue carousel, in: 8th RILEM International Conference on Mechanisms of Cracking and Debonding in Pavements, Springer Netherlands, Dordrecht, 2016, pp. 749–755.

[12] H. Liu, Z. Deng, F. Han, Y. Xia, Q. H. Liu, M. Sato, Time-frequency analysis of air-coupled gpr data for identification of delamination between pavement layers, Construction and Building Materials 154 (2017) 1207 – 1215. doi:10.1016/j.conbuildmat.2017.06.132.

[13] Z. Zyada, T. Matsuno, Y. Hasegawa, S. Sato, T. Fukuda, Advances in gpr-based landmine automatic detection, Journal of the Franklin Institute 348 (1) (2011) 66 – 78, mechatronics and its Applications. doi:10.1016/j.jfranklin.2009.02.014.

[14] M. A. Gonzalez-Huici, F. Giovanneschi, A combined strategy for landmine detection and identification using synthetic gpr responses, Journal of Applied Geophysics 99 (2013) 154 – 165. doi:10.1016/j.jappgeo.2013.08.006.

[15] M. Shaw, S. Millard, T. Molyneaux, M. Taylor, J. Bungey, Location of steel reinforcement in concrete using ground penetrating radar and neural networks, NDT and E International 38 (3) (2005) 203 – 212, structural Faults and Repair. doi:https://doi.org/10.1016/j.ndteint.2004.06.011.

[16] B. Sangoju, Estimation of rebar diameter in concrete structural elements using ground penetrating radar.

[17] Y.-F. Shih, Y.-R. Wang, S.-S. Wei, C.-W. Chen, Improving non-destructive test results using artificial neural networks, International Journal of Machine Learning and Computing 5 (6) (2015) 480.

[18] C. Wunderlich, C. Tschöpe, F. Duckhorn, Advanced methods in nde using machine learning approaches, AIP Conference Proceedings 1949 (1) (2018) 020022. doi:10.1063/1.5031519.

[19] A. Jafarian, S. M. Nia, A. K. Golmankhaneh, D. Baleanu, On artificial neural networks approach with new cost functions, Applied Mathematics and Computation 339 (2018) 546 – 555. doi:https://doi.org/10.1016/j.amc.2018.07.053.

[20] D. Berrar, Bayes' theorem and naive bayes classifier, in: S. Ranganathan, M. Gribskov, K. Nakai, C. Schönbach (Eds.), Encyclopedia of Bioinformatics and Computational Biology, Academic Press, Oxford, 2019, pp. 403 – 412. doi:https://doi.org/10.1016/B978-0-12-809633-8.20473-1.

[21] S. D. Vito, G. Fattoruso, M. Pardo, F. Tortorella, G. D. Francia, Semi-supervised learning techniques in artificial olfaction: A novel approach to classification problems and drift counteraction, IEEE Sensors Journal 12 (11) (2012) 3215–3224. doi:10.1109/JSEN.2012.2192425.

[22] J.-M. Simonin, V. Baltazart, P. Hornych, J.-P. Kerzrého, X. Dérobert, S. Trichet, O. Durand, J. Alexandre, A. Joubert, Detection of debonding and vertical cracks with nd techniques during accelerated tests, in: 4th International conference on Accelerated Pavement Testing (APT), Davis, California, USA, 2012.

[23] J.-M. Simonin, C. Fauchard, P. Hornych, V. Guilbert, J.-P. Kerzrého, S. Trichet, Detecting unbounded interface with non destructive techniques,, in: A.-Q. I. A. L. Scarpas A., Kringos N. (Ed.), 7th RILEM International Conference on Mechanisms on Cracking and Debonding in Pavements, Springer Netherlands, Dordrecht, 2012.

[24] Z. Dong, S. Ye, Y. Gao, G. Fang, X. Zhang, Z. Xue, T. Zhang, Rapid detection methods for asphalt pavement thicknesses and defects by a vehicle-mounted ground penetrating radar (gpr) system, Sensors 16 (12). doi:10.3390/s16122067.

[25] D. Seyfried, J. Schoebel, Stepped-frequency radar signal processing, Journal of Applied Geophysics 112 (2015) 42 – 51. doi:10.1016/j.jappgeo.2014.11.003.

[26] C. Diakité, N. Fortino, J.-Y. Dauvignac, Antenne ETSA "Exponential Tapered Slot Antenna" miniature pour radar à pénétration de surface, in: 19èmes Journées Nationales Microondes (JNM 2015), 19èmes Journées Nationales Microondes (JNM 2015), Bordeaux, France, 2015, pp. Session Antennes large bande et multibandes C3L–D, papier 9337.

[27] X. Dérobert, V. Baltazart, Report on step-frequency radar data collection on the fatigue carousel: Personal communication (2012).

[28] H. Chung, D. Lawton, Frequency characteristics of seismic reflections from thin beds, Canadian Journal of Exploration Geophysics 31 (1) (1995) 32–37.

[29] D. Arosio, Rock fracture characterization with gpr by means of deterministic deconvolution, Journal of Applied Geophysics 126 (2016) 27 – 34. doi:https://doi.org/10.1016/j.jappgeo.2016.01.006.

[30] J. H. Bradford, J. C. Deeds, Ground-penetrating radar theory and application of thin-bed offset-dependent reflectivity, GEOPHYSICS 71 (3) (2006) K47–K57. doi:10.1190/1.2194524.

[31] Y. Liu, D. R. Schmitt, Amplitude and avo responses of a single thin bed, GEOPHYSICS 68 (4) (2003) 1161–1168. doi:10.1190/1.1598108.

[32] A. Shakas, N. Linde, Effective modeling of ground penetrating radar in fractured media using analytic solutions for propagation, thin-bed interaction and dipolar scattering, Journal of Applied Geophysics 116 (2015) 206 – 214. doi:https://doi.org/10.1016/j.jappgeo.2015.03.018.

[33] A. Shakas, N. Linde, Apparent apertures from ground penetrating radar data and their relation to heterogeneous aperture fields, Geophysical Journal International 209 (3) (2017) 1418–1430. doi:10.1093/gji/ggx100.

[34] L. Sambuelli, C. Calzoni, Estimation of thin fracture aperture in a marble block by gpr sounding., Bollettino di Geofisica Teorica ed Applicata 51 (2-3) (2010) 239 – 252.

[35] C. L. Bastard, V. Baltazart, Y. Wang, J. Saillard, Thin-pavement thickness estimation using gpr with high-resolution and superresolution methods.(ground-penetrating radar), IEEE Transactions on Geoscience and Remote Sensing 45 (8) (2007-08-01) 2511(9).

[36] V. N. Vapnik, The Nature of Statistical Learning Theory, Springer-Verlag New York, Inc., New York, NY, USA, 1995.

[37] E. Alpaydin, Introduction to Machine Learning, Cambridge, MA: The MIT Press, 2014.

[38] B. E. Boser, I. M. Guyon, V. N. Vapnik, A training algorithm for optimal margin classifiers, in: Proceedings of the Fifth Annual Workshop on Computational Learning Theory, COLT '92, ACM, New York, NY, USA, 1992, pp. 144–152. doi:10.1145/130385.130401.

[39] V. Vapnik, Pattern recognition using generalized portrait method, Automation and Remote Control 24 (1963) 774–780.

[40] C.-C. Chang, C.-J. Lin, LIBSVM: A library for support vector machines, ACM Transactions on Intelligent Systems and Technology 2 (2011) 27:1–27:27.

[41] G. C. Cawley, N. L. Talbot, On over-fitting in model selection and subsequent selection bias in performance evaluation, J. Mach. Learn. Res. 11 (2010) 2079–2107.

[42] A. B. Gonçalves, J. S. Souza, G. G. d. Silva, M. P. Cereda, A. Pott, M. H. Naka, H. Pistori, Feature extraction and machine learning for the classification of brazilian savannah pollen grains, PLOS ONE 11 (6) (2016) 1–20. doi:10.1371/journal.pone.0157044.

[43] G. Kumar, P. K. Bhatia, A detailed review of feature extraction in image processing systems, in: 2014 Fourth International Conference on Advanced Computing Communication Technologies, 2014, pp. 5–12. doi:10.1109/ACCT.2014.74.

[44] F. Samadzadegan, H. Hasani, T. Partovi, Sensitivity analysis of support vector machine in classification of hyperspectral imagery, in: Proceedings of the Canadian Geomatics Conference, Calgary, Canada, 2010.

[45] H. Liu, H. Motoda, R. Setiono, Z. Zhao, Feature selection: An ever evolving frontier in data mining, in: H. Liu, H. Motoda, R. Setiono, Z. Zhao (Eds.), Proceedings of the Fourth International Workshop on Feature Selection in Data Mining, Vol. 10 of Proceedings of Machine Learning Research, PMLR, Hyderabad, India, 2010, pp. 4–13.

[46] T. K. Roy, M. Morshed, Performance analysis of low pass fir filters design using kaiser, gaussian and tukey window function methods, in: 2013 2nd International Conference on Advances in Electrical Engineering (ICAEE), 2013, pp. 1–6. doi:10.1109/ICAEE.2013.6750294.

[47] M. S. El-Mahallawy, M. Hashim, Material classification of underground utilities from gpr images using dct-based svm approach, IEEE Geoscience and Remote Sensing Letters 10 (6) (2013) 1542–1546. doi:10.1109/LGRS.2013.2261796.

[48] X. Xie, H. Qin, C. Yu, L. Liu, An automatic recognition algorithm for gpr images of rc structure voids, Journal of Applied Geophysics 99 (2013) 125 – 134. doi:10.1016/j.jappgeo.2013.02.016.

[49] S. Shihab, W. Al-Nuaimy, Y. Huang, A. Eriksen, Neural network target identifier based on statistical features of GPR signals, in: Society of Photo-Optical Instrumentation Engineers (SPIE) Conference Series, Vol. 4758, 2002, pp. 135–138. doi:10.1117/12.462228.

[50] R. M. G. Tello, T. Bastos-Filho, A. Frizera-Neto, S. Arjunan, D. K. Kumar, Feature extraction and classification of semg signals applied to a virtual hand prosthesis, in: 2013 35th Annual International Conference of the IEEE Engineering in Medicine and Biology Society (EMBC), 2013, pp. 1911–1914. doi:10.1109/EMBC.2013.6609899.

[51] K. K. Patro, P. R. Kumar, Effective feature extraction of ecg for biometric application, Procedia Computer Science 115 (2017) 296 – 306, 7th International Conference on Advances in Computing and Communications, ICACC-2017, 22-24 August 2017, Cochin, India. doi:10.1016/j.procs.2017.09.138.

[52] W. Lu, H. Hou, J. Chu, Feature fusion for imbalanced ecg data analysis, Biomedical Signal Processing and Control 41 (2018) 152 – 160. doi:10.1016/j.bspc.2017.11.010.

[53] Y. Bengio, A. Courville, P. Vincent, Representation learning: A review and new perspectives, IEEE

Transactions on Pattern Analysis and Machine Intelligence 35 (8) (2013) 1798–1828. doi:10.1109/TPAMI.2013.50.

[54] F. Song, Z. Guo, D. Mei, Feature selection using principal component analysis, in: 2010 International Conference on System Science, Engineering Design and Manufacturing Informatization, Vol. 1, 2010, pp. 27–30. doi:10.1109/ICSEM.2010.14.

[55] M. Kallakech, P. Biela, L. Macaire, D. Hamad, Constraint scores for semi-supervised feature selection: A comparative study, Pattern Recognition Letters 32 (5) (2011) 656–665. doi:10.1016/j.patrec.2010.12.014.

[56] X. Zeng, Y. Chen, C. Tao, D. v. Alphen, Feature selection using recursive feature elimination for handwritten digit recognition, in: 2009 Fifth International Conference on Intelligent Information Hiding and Multimedia Signal Processing, 2009, pp. 1205–1208. doi:10.1109/IIH-MSP.2009.145.

[57] M. P. Sampat, Z. Wang, S. Gupta, A. C. Bovik, M. K. Markey, Complex wavelet structural similarity: A new image similarity index, IEEE Transactions on Image Processing 18 (11) (2009) 2385–2401. doi:10.1109/TIP.2009.2025923.

[58] F. Friedrichs, C. Igel, Evolutionary tuning of multiple svm parameters, Neurocomputing 64 (2005) 107 – 117, trends in Neurocomputing: 12th European Symposium on Artificial Neural Networks 2004. doi:https://doi.org/10.1016/j.neucom.2004.11.022.

[59] K.-Q. Shen, C.-J. Ong, X.-P. Li, E. P. V. Wilder-Smith, Feature selection via sensitivity analysis of svm probabilistic outputs, Machine Learning 70 (1) (2008) 1–20. doi:10.1007/s10994-007-5025-7.

[60] C. A. M. Lima, C. Junqueira, R. Suyama, F. J. V. Zuben, J. M. T. Romano, Least-squares support vector machines for doa estimation: a step-by-step description and sensitivity analysis, in: Proceedings. 2005 IEEE International Joint Conference on Neural Networks, 2005., Vol. 5, 2005, pp. 3226–3231 vol. 5. doi:10.1109/IJCNN.2005.1556444.

[61] I. E. A. Rueda, F. A. Arciniegas, M. J. Embrechts, Svm sensitivity analysis: an application to currency crises aftermaths, IEEE Transactions on Systems, Man, and Cybernetics - Part A: Systems and Humans 34 (3) (2004) 387–398. doi:10.1109/TSMCA.2004.824850.

[62] A. Subasi, M. I. Gursoy, Eeg signal classification using pca, ica, lda and support vector machines, Expert Systems with Applications 37 (12) (2010) 8659 – 8666. doi:https://doi.org/10.1016/j.eswa.2010.06.065.

[63] F. Melgani, Y. Bazi, Classification of electrocardiogram signals with support vector machines and particle swarm optimization, IEEE Transactions on Information Technology in Biomedicine 12 (5) (2008) 667–677. doi:10.1109/TITB.2008.923147.

[64] T.-K. Lin, Pca/svm-based method for pattern detection in a multisensor system, Mathematical Problems in Engineering 2018 (2018) 1–11. doi:10.1155/2018/6486345.

[65] A. Saltelli, M. Ratto, T. Andres, F. Campolongo, J. Cariboni, D. Gatelli, M. Saisana, S. Tarantola, Global sensitivity analysis: the primer, John Wiley and Sons, 2008.

[66] M. Pal, G. M. Foody, Feature selection for classification of hyperspectral data by svm, IEEE Transactions on Geoscience and Remote Sensing 48 (5) (2010) 2297–2307. doi:10.1109/TGRS.2009.2039484.

[67] V. Sharma, D. Baruah, D. Chutia, P. Raju, D. K. Bhattacharya, An assessment of support vector machine kernel parameters using remotely sensed satellite data, in: 2016 IEEE International Conference on Recent Trends in Electronics, Information Communication Technology (RTEICT), 2016, pp. 1567–1570. doi:10.1109/RTEICT.2016.7808096.

[68] R. Palaniappan, K. Sundaraj, S. Sundaraj, A comparative study of the svm and k-nn machine learning algorithms for the diagnosis of respiratory pathologies using pulmonary acoustic signals, BMC bioinformatics 15 (1) (2014) 223.

[69] B. Waske, S. van der Linden, J. A. Benediktsson, A. Rabe, P. Hostert, Sensitivity of support vector machines to random feature selection in classification of hyperspectral data, IEEE Transactions on Geoscience and Remote Sensing 48 (7) (2010) 2880–2889. doi:10.1109/TGRS.2010.2041784.

[70] K. K. Dobbin, R. M. Simon, Optimally splitting cases for training and testing high dimensional classifiers, BMC medical genomics 4 (1) (2011) 31.

[71] M. T. Hagan, H. B. Demuth, M. H. Beale, O. De Jesús, Neural network design, Vol. 20, Pws Pub. Boston, 1996.

[72] V. Gholami, K. Chau, F. Fadaee, J. Torkaman, A. Ghaffari, Modeling of groundwater level fluctuations using dendrochronology in alluvial aquifers, Journal of Hydrology 529 (2015) 1060 – 1069. doi:https://doi.org/10.1016/j.jhydrol.2015.09.028.

[73] P. Niżewski, J. Dach, P. Boniecki, Zastosowanie sztucznych sieci neuronowych do modelowania procesu emisji amoniaku z pól nawożonych gnojowicą, Inżynieria Rolnicza 11 (2007) 235–242.

[74] M. Kuhn, K. Johnson, Applied predictive modeling, Vol. 26, New York, NY: Springer, 2013.